

Effective Spectral Unmixing via Robust Representation and Learning-based Sparsity

Feiyun Zhu, Ying Wang, Bin Fan, Gaofeng Meng and Chunhong Pan

Abstract—Hyperspectral unmixing (HU) plays a fundamental role in a wide range of hyperspectral applications. It is still challenging due to the common presence of outlier channels and the large solution space. To address the above two issues, we propose a novel model by emphasizing both robust representation and learning-based sparsity. Specifically, we apply the $\ell_{2,1}$ -norm to measure the representation error, preventing outlier channels from dominating our objective. As a result, the side effects of outlier channels are largely relieved. Besides, we observe that the mixed level of each pixel varies over image grids. Based on this observation, we exploit a learning-based sparsity method to simultaneously learn the HU results and a sparse guidance map. Via this guidance map, the sparsity constraint in the ℓ_p ($0 < p \leq 1$)-norm is adaptively imposed according to the mixed level of each pixel. Compared with state-of-the-art methods, our model is better suited to the real situation, thus expected to achieve better HU results. The resulted objective is highly non-convex and non-smooth, and so it is hard to optimize. As a profound theoretical contribution, we propose an efficient algorithm to solve it. Meanwhile, the convergence proof and the computational complexity analysis are systematically provided. Extensive evaluations verify that our method is highly promising for the HU task—it achieves very accurate guidance maps and much better HU results compared with state-of-the-art methods.

Index Terms—Robust Representation and Learning-based Sparsity (RRLbS), Sparse guided Map, Mixed Pixel, Hyperspectral Unmixing (HU), Hyperspectral Visualization.

I. INTRODUCTION

HYPERSPECTRAL unmixing (HU) is one of the most foundation steps for various applications, such as sub-pixel mapping [1], high-resolution hyperspectral imaging [2], hyperspectral enhancement [3], hyperspectral compression and reconstruction [4], hyperspectral visualization and understanding [5, 6], detection and identification substances in the scene [3, 7] etc. The goal of HU is to break down each pixel spectrum into a set of “pure” spectra (called *endmembers* such as the spectra of water, grass, tree etc.), weighted by the corresponding proportions, called *abundances*. Formally, HU methods take in a hyperspectral image with L channels and N pixels [8], and assume that each pixel $\mathbf{x} \in \mathbb{R}_+^L$ is a composite of K *endmembers* $\{\mathbf{m}_k\}_{k=1}^K \in \mathbb{R}_+^L$. Specifically, the linear combinatorial model is the most popular one

$$\mathbf{x} = \sum_{k=1}^K \mathbf{m}_k a_k, \quad \text{s.t. } a_k \geq 0 \text{ and } \sum_{k=1}^K a_k = 1, \quad (1)$$

Feiyun Zhu, Ying Wang, Bin Fan, Gaofeng Meng and Chunhong Pan are with the National Laboratory of Pattern Recognition, Institute of Automation, Chinese Academy of Sciences (e-mail: fy Zhu0915@gmail.com and {ywang, bfan, gfmeng and chpan}@nlpr.ia.ac.cn).

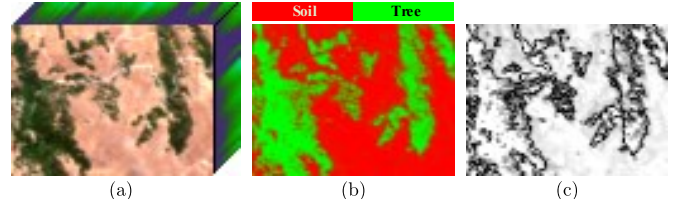


Figure 1. As the mixed level of each pixel varies over image grids, the sparse constraint should be individually imposed according to the mixed level of each pixel, rather than roughly imposed at the same strength for all the pixels. (a) hyperspectral image of two substances: soil and tree. (b) *abundance* map. (c) is the guided map exhibiting the individually mixed level of each pixel—the darker indicates the more mixed. (best viewed in color)

where a_k is the composite *abundance* of the k^{th} *endmember*. In the unsupervised setting, both *endmembers* $\{\mathbf{m}_k\}_{k=1}^K$ and *abundances* $\{a_k\}_{k=1}^K$ are unknown. Such case makes the objective function non-convex and the solution space very large [6, 9]. Therefore, reasonable prior knowledge is required to restrict the solution space, and moreover to bias the solution toward good stationary points.

To reduce the solution space, various constraints are imposed upon the *abundance* [7, 9–12] as well as upon the *endmember* [13, 14]. Although, these methods work to some extent, they are far from the optimal for the following two reasons. First, the side effects of badly degraded channels are generally ignored in state-of-the-art methods. Many degraded channels deviate significantly from the majority of hyperspectral channels. The objective of state-of-the-art methods is easily dominated by the outlier channel, leading to poor unmixing performances. Second, almost all existing constraints are roughly imposed at the same strength for all the factors. Such implementation does not meet the practical situation; an example is illustrated in Fig. 1, where the mixed level of each pixel varies over image grids. Therefore, it is more reasonable to impose an individual strength of sparse constraints according to the mixed level of each pixel, rather than roughly impose the same strength of sparse constraints for all the pixel. Please refer to the footnote¹ for the detailed explanation of the relationship between mixing pixel and sparsity.

Indeed, there is one method [6] imposing the adaptively sparse constraint for each pixel. However, [6] proposed a heuristic method to learn the guided map which is ineffective and inaccurate for the vast smooth areas in the image.

¹Note that the mixed level of a pixel \mathbf{x}_n is negatively correlated with the sparse level of the corresponding *abundance* \mathbf{a}_n . If pixel \mathbf{x}_n is very “pure”, the *abundance* \mathbf{a}_n will be highly sparse and vice versa. For example in Fig. 1, the *abundances* are [0.5, 0.5] and [0, 9, 0.1] respectively for pixel \mathbf{y}_i and \mathbf{y}_j . Then \mathbf{y}_i is more mixed and less sparser than \mathbf{y}_j .

Accordingly, the sparse constraint is inaccurate. It is expected that the more accurate constraints would bias the solution to the more satisfactory local minima.

To alleviate the above issues, we propose a novel method, named effective spectral unmixing via robust representation and learning-based sparsity (RRLbS) for the HU task. Specifically, the $\ell_{2,1}$ -norm is employed to measure the representation loss, preventing large errors from dominating our objective. In this way, the robustness against outlier channels is greatly enhanced. Besides, a learning-based sparsity method is exploited to individually impose the sparsity constraint according to the mixed level of each pixel. The main contributions of this work are summarized as follows.

- It is the side influences of badly degraded channels that are generally ignored in the state-of-the-art methods. To the best of our knowledge, this is the first attempt in the HU field to propose the $\ell_{2,1}$ -norm based robust model to relieve the side effects of outlier channels.
- Besides, we propose a novel learning-based sparsity method to simultaneously learn the HU results and a guided map. The method to estimate the guided map is novel and effective. Through this guided map, the mixed level of every pixel is described and respected by imposing an adaptive sparsity constraint according to the mixed level of each pixel. Such implementation helps to achieve highly promising HU results and guided maps.
- We propose an efficient algorithm to solve the joint $\ell_{2,1}$ -norm and ℓ_p -norm based objective, which is highly non-convex, non-smooth and challenging to solve. Both theoretical and empirical analyses are conducted to verify its convergence property. Besides, the computational complexity analysis is systematically analyzed as well.

The rest of this paper is organized as below: in Section II, the related HU work is systematically reviewed. Section III presents the new model (RRLbS) and its physical motivations. The algorithm as well its theoretical convergence proof and computational complexity analysis are given in Section IV. Then, extensive evaluations are provided in Section V. Finally, the conclusion of this work is drawn in Section VI.

II. PREVIOUS WORK

The existing HU methods are typically categorized into three types: supervised methods [3, 4], weakly supervised methods [15, 16] and unsupervised methods [7, 10, 14, 17–19] (Here the definitions of supervised, weakly supervised are very different from the definition in machine learning [20–28]. Please refer to the following paragraphs for their new definitions). For the supervised methods, the *endmembers* are given in advance; only the *abundances* need to estimate. Although in this way, the HU problem is greatly simplified, it is usually inconvenient or intractable to obtain feasible *endmembers* in the supervised setting, thus, hampering the acquisition of good estimations.

Accordingly, the weakly supervised methods [15, 16] are a type of popular methods. A large library of substance spectra have been collected by a field spectrometer beforehand. Then, the HU task becomes the problem of finding the optimal subset

of spectra in the library that can best represent all pixels in the scene [15]. Unfortunately, the library is far from optimal for the fact that the spectra in it are not standardly unified. First, for different hyperspectral sensors, the spectral shape of the same substance are greatly inconsistent. Second, for various hyperspectral images, the length of pixel spectra is largely different as well—for example some images have 115 channels, while another has 224 channels and some even have 480 spectral channels. Their electromagnetic spectra ranges are also very different. Finally, the recording conditions are highly different as well—some hyperspectral images are captured far from the outer space, while some hyperspectral images are obtained from the airplane or ground. Due to the atmospheric effects etc., the different recording condition would lead to different spectral appearances. In short, the weakness of the library brings side effects on this kind of methods.

More commonly, the *endmembers* are selected from the image itself to ensure the spectral consistency [3] and the unsupervised HU methods are preferred. The unsupervised HU methods could be generally categorized into two types: geometric methods [29–34] and statistical ones [6, 19, 35–39]. The geometric methods usually exploit the simplex to model the distribution of spectral pixels. Perhaps, N-FINDR [40] and Vertex Component Analysis (VCA) [30] are the most typical geometric methods. For N-FINDR, the *endmembers* are extracted by inflating a simplex inside the hyperspectral pixel distribution and treating the vertices of a simplex with the largest volume as *endmembers* [40]. VCA [30] projects all pixels onto a direction orthogonal to the simplex spanned by the chosen *endmembers*; the new *endmember* is identified as the extreme of the projection. Although these methods are simple and fast, they suffer from the requirement of pure pixels, which is usually unreliable in practice [7, 10, 41].

Accordingly, many statistical methods have been proposed for or applied to the HU problem, among which the Non-negative Matrix Factorization (NMF) [42] and its extensions are the most popular. The goal of NMF is to find two nonnegative matrices to approximate the original matrix with their product [12]. There are two valuable reasons to apply the nonnegative constraint on both factor matrices. First, both *endmembers* and *abundances* should be nonnegative. Such case means that the NMF model is physically suited to the HU task. Second, the nonnegative constraint only allows for additive combinations, not subtractions, yielding a parts-based representation [12]. This parts-based property enables factor results more intuitive and interpretable, as existing studies on psychological and physiological field have shown human brain also works in the parts-based manner [43, 44].

Although NMF is well adapted to applications of face analysis [45, 46] and documents clustering [47, 48], the objective function is non-convex, naturally resulting in a large solution space [49]. Many extensions have been proposed by employing all kinds of priors to restrict the solution space. For the HU task, the priors are imposed either upon *abundances* [7, 9, 11] or upon *endmembers* [13, 14]. For example, the Local Neighborhood Weights regularized NMF method [11] (W-NMF) assumes that the hyperspectral pixels are distributed on a manifold structure and exploits appropriate

weights in the local neighborhood to enhance the spectral and spatial information [50]. This information could be eventually transferred to the *abundance* space via the Laplace graph constraint. Actually, this constraint has a smooth impact. It will weaken the parts-based property of NMF.

Inspired by MVC-NMF [13], Wan *et al.* [14] proposed the EDC-NMF method. The basic assumption is originated from two perspectives. First, due to the high spectral resolution of hyperspectral sensors, the *endmember* signal should be smooth itself. Besides, the *endmember* signals should possess distinct shapes so that we can separate out different materials [3]. However, in their algorithm, they take a derivative along the *endmember* vector, introducing negative values to the updating rule. To make up this drawback, the elements in the *endmember* matrix are required to project to a given nonnegative value after each iteration. Consequently, the regularization parameters could not be chosen freely, which limits the efficacy of this method.

The sparsity-based methods are the most successful methods for the HU task. They assume that in hyperspectral images most pixels are mixed by a subset of *endmembers*, rather than all *endmembers*, thus employing various kinds of sparse constraints on *abundances*. Specifically, the $\ell_{1/2}$ -NMF [7] is a state of the art sparsity regularized NMF method that is derived from Hoyer's lasso regularized NMF [51]. The lasso constraint [52, 53] could not enforce further sparse when the full additivity constraint is used, limiting the effectiveness of this method [7]. Thus, Qian *et al.* exploits the ℓ_p ($p = 1/2$)-norm to regularize the *abundances* as it has been proved by Fan *et al.* [54] that the ℓ_p ($p = 1/2$) constraint could obtain sparser solutions than the ℓ_1 -norm does.

Although the related methods work to some extent, they are far from the optima. Thus, we propose a new method by emphasizing both robust representation and learning-based sparsity. Through the former, the side effects of outlier channels are greatly relieved. While via the latter, it is more likely to bias the HU solution to some suited stationary points in the large solution space.

III. RRLBS: ROBUST REPRESENTATION AND LEARNING-BASED SPARSITY

In this section, we propose a novel model by emphasizing both robust representation and learning-based sparsity. To relieve the side influences of badly degraded channels, the $\ell_{2,1}$ -norm, rather than ℓ_2 -norm, is employed to measure the representation loss, preventing too large errors from dominating our objective. Then, a learning-based sparsity method is proposed to update a guidance map, by which the sparse constraint could be individually imposed according to the mixed level of each pixel. Such implementation is more reasonable, thus expected to get better HU results.

Notation. In this paper, we use boldface uppercase letters to denote matrices and boldface lowercase letters to represent vectors. Given a matrix $\mathbf{X} \triangleq \{X_{ln}\} \in \mathbb{R}^{L \times N}$, we denote the l^{th} row and n^{th} column as $\mathbf{x}^l \in \mathbb{R}^{1 \times N}$ and $\mathbf{x}_n \in \mathbb{R}^L$ respectively. X_{ln} is the (l, n) -th entry in the matrix. A nonnegative

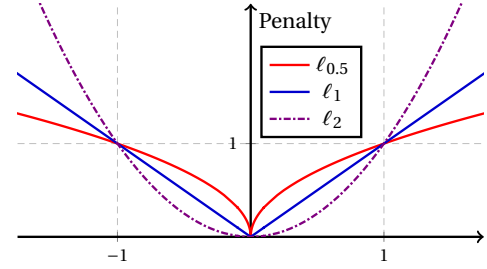


Figure 2. ℓ_p ($0.5 \leq p \leq 1$)-norm versus ℓ_2 -norm in shape. Compared with the ℓ_2 -norm, ℓ_1 is more capable of preventing large errors from dominating the objective energy. Compared with the ℓ_1 sparse constraint, ℓ_p ($0.5 \leq p < 1$) tends to find a sparser solution [7, 54, 57].

matrix is denoted as $\mathbf{X} \geq \mathbf{0}$ or $\mathbf{X} \in \mathbb{R}_+^{L \times N}$. The $\ell_{2,1}$ -norm of matrices is defined as $\|\mathbf{X}\|_{2,1} = \sum_l^L \left(\sum_n^N X_{ln}^2 \right)^{1/2}$.

Problem formalization. In the HU problem, we are often given a hyperspectral image of N pixels and L channels, which is denoted by a nonnegative matrix $\mathbf{X} \triangleq [\mathbf{x}_1, \mathbf{x}_2, \dots, \mathbf{x}_N] \in \mathbb{R}_+^{L \times N}$. From the linear mixture perspective, the goal of HU is to find two nonnegative matrices to well approximate \mathbf{X} with their product. Formally, the discrepancy between \mathbf{X} and its representation $\tilde{\mathbf{X}}$ is modeled as

$$\min_{\mathbf{M}, \mathbf{A}} \text{loss} \{ \mathbf{X}, \tilde{\mathbf{X}} \}, \quad \text{s.t. } \tilde{\mathbf{X}} = \mathbf{M}\mathbf{A}, \mathbf{M} \geq \mathbf{0}, \mathbf{A} \geq \mathbf{0}, \quad (2)$$

where $\mathbf{M} \triangleq [\mathbf{m}_1, \dots, \mathbf{m}_K] \in \mathbb{R}_+^{L \times K}$ is the *endmember* matrix including K spectral bases, $K \ll \min\{L, N\}$; $\mathbf{A} \triangleq [\mathbf{a}_1, \dots, \mathbf{a}_N] \in \mathbb{R}_+^{K \times N}$ is the corresponding *abundance* matrix—the n^{th} ($\forall n = 1, \dots, N$) column vector \mathbf{a}_n contains all K *abundances* at pixel \mathbf{x}_n ; $\text{loss} \{ \cdot, \cdot \}$ is a loss function measuring the difference between two terms. When setting $\text{loss} \{ \cdot, \cdot \}$ as the Euclidean loss, the objective (2) becomes the standard NMF problem [6, 42, 49], which is commonly used in a great number of state of the art HU methods [6, 7, 9, 10, 13, 14]. However, the Euclidean loss is prone to outliers [55, 56]. Accordingly, our initial goal is to propose a robust HU model.

A. Robust Representation in the $\ell_{2,1}$ -norm

Existing HU methods generally use the Euclidean loss to measure the representation error, that is

$$\min_{\mathbf{M}, \mathbf{A}} \sum_{l=1}^L \|\mathbf{x}^l - \mathbf{m}^l \mathbf{A}\|_2^2, \quad \text{s.t. } \mathbf{M} \geq \mathbf{0}, \mathbf{A} \geq \mathbf{0}, \quad (3)$$

where \mathbf{x}^l is the l^{th} channel (i.e. row vector) in \mathbf{X} ; \mathbf{m}^l is the l^{th} channel in \mathbf{M} . Similar to the existing least square minimization based models in machine learning and statistics [58, 59], (3) is sensitive to the presence of outlier channels [56, 60, 61]. However, from the perspective of remote sensing, hyperspectral images are very likely to contain outlier channels. This is owing to the following two reasons. First, due to the high spectral resolution of hyperspectral sensors, it receives very litter energy from a narrow wavelength range when producing each hyperspectral channel. In this way, the imaging information is highly easy to be overwhelmed by various kinds

of noises. Second, the bad imaging conditions are responsible for the degraded channels as well—when imaging from the outer space or airplanes, due to the water vapor and the atmospheric effects etc., the hyperspectral channels are easy to be blank or badly noised. Specifically, many noised channels deviate significantly from the majority of the hyperspectral channels. They are actually outlier channels.

To identify the outlier channels and to relieve the side effects they cause, a robust loss in the $\ell_{2,1}$ -norm is proposed

$$\min_{\mathbf{M}, \mathbf{A}} \sum_{l=1}^L \|\mathbf{x}^l - \mathbf{m}^l \mathbf{A}\|_2, \quad \text{s.t. } \mathbf{M} \geq \mathbf{0}, \mathbf{A} \geq \mathbf{0}. \quad (4)$$

Considering all the row vectors together, the objective (4) becomes the concise matrix format:

$$\min_{\mathbf{M}, \mathbf{A}} \|\mathbf{X} - \mathbf{M}\mathbf{A}\|_{2,1}, \quad \text{s.t. } \mathbf{M} \geq \mathbf{0}, \mathbf{A} \geq \mathbf{0}, \quad (5)$$

In our new model, the $\ell_{2,1}$ -norm is applied to the representation loss—the ℓ_1 -norm is imposed among channels and the ℓ_2 -norm is used for pixels. As the ℓ_1 -loss is capable of preventing large representation errors to dominate the objective, as shown in Fig. 2. The side effects of outlier channels are greatly reduced and the robustness of the HU task is enhanced.

B. Learning-based Sparsity Constraint via the Guidance Map

State-of-the-art methods generally impose an identical strength of sparsity constraints for all the pixels, e.g.,

$$\mathcal{J}(\mathbf{A}) = \sum_{n=1}^N h_n \|\mathbf{a}_n\|_1, \quad \mathcal{J}(\mathbf{A}) = \sum_{n=1}^N h_n \|\mathbf{a}_n\|_{1/2}^{1/2},$$

where $\{h_n = 1\}_{n=1}^N$ is the guided value for both ℓ_1 -NMF [51] and $\ell_{1/2}$ -NMF [7]. However, the mixed level of each pixel varies over image grids, as shown in Fig. 1. It is more reasonable to impose an individual sparsity constraint according to the mixed level of each pixel. To this end, we propose an iterative method to learn a guidance map $\mathbf{h} \in \mathbb{R}_+^N$, by which the sparsity constraint in the ℓ_p ($0.5 \leq p \leq 1$)-norm will be individually applied as

$$\mathcal{J}(\mathbf{A}) = \sum_{n=1}^N \|\mathbf{a}_n\|_{1-h_n}^{1-h_n} = \sum_{n=1}^N \sum_{k=1}^K |A_{kn}|^{1-H_{kn}}, \quad (6)$$

where $\|\mathbf{a}\|_p^p = \sum_k |a_k|^p$, h_n is the n^{th} entry in the guided map \mathbf{h} , reflecting the mixed level of the n^{th} pixel; H_{kn} is the (k, n) -th element in the matrix $\mathbf{H} = \mathbf{1}_K \mathbf{h}^T$; $\mathbf{1}_K$ is the column vector of all ones with length K . For each pixel \mathbf{x}_n , the choice of p is solely dependent upon the corresponding guidance value h_n , performing a nonlinearly weighting role for the sparsity constraint upon \mathbf{a}_n . Specifically, as the sparsity of ℓ_p solution increases as p decreases [7, 54, 57], a smaller

²Fan et al. has shown that the sparsity of ℓ_p ($0.5 \leq p \leq 1$) solution increases as p decreases, whereas the sparsity of the solution of ℓ_p ($0 < p \leq 0.5$) shows little change with respect to p [7, 54]. Thus, to ensure the sensitivity of the individually sparsity constraint, it is sufficient to use the ℓ_p ($0.5 \leq p \leq 1$)-norm in our model.

$1 - h_n$ ($\forall n = 1, 2, \dots, N$) will impose a stronger sparse constraint on \mathbf{a}_n . In this way, the sparse constraint is individually imposed for each pixel. The matrix format of (6) is

$$\mathcal{J}(\mathbf{A}) = \|\mathbf{A}^{1-\mathbf{H}}\|_1, \quad (7)$$

where $\mathbf{A}^{1-\mathbf{H}} = \left[(A_{kn})^{1-H_{kn}} \right] \in \mathbb{R}_+^{K \times N}$ is an element-wise exponential operation.

The remaining problem is how to learn the optimal guidance map $\mathbf{h}^* \in \mathbb{R}_+^N$. In [6], there is one heuristic method to learn the guided map, which is effective in the transitional areas. However, it is ineffective in the vast smooth areas in the image due to the heuristic mechanism. An inaccurate guided map would lead to an unsuitable sparse constraint. In this paper, we find that \mathbf{h}^* is crucially dependent upon the mixed level of each pixel, i.e., the sparse level of the optimal *abundance* \mathbf{A}^* . In other words, if pixel \mathbf{x}_n is highly mixed (i.e. the *abundance* \mathbf{a}_n^* is weakly sparse), h_n will be small; once \mathbf{x}_n is highly “pure” (i.e. \mathbf{a}_n^* is largely sparse), h_n will be large. However, the mixed level of each pixel is unavailable due to the unknown of the optimal *abundance*.

To achieve a good guidance map, here we will propose a two-step strategy. First, a heuristic strategy is used to get an initial guess. Then a learning-based updating rule is exploited to generate a sequence of improved estimates until they reach a stable solution. We observe that pixels in the transition area or image edges are very likely to be highly mixed [6]. Accordingly, we propose a heuristic strategy to get an initial guidance map:

$$h_i = \sum_{j \in \mathcal{N}_i} s_{ij}, \quad \forall i \in \{1, 2, \dots, N\}, \quad (8)$$

where \mathcal{N}_i is the neighborhood of \mathbf{x}_i that includes four neighbors; s_{ij} is a similarities measured as

$$s_{ij} = \exp\left(-\frac{\|\mathbf{x}_j - \mathbf{x}_i\|_2^2}{\sigma}\right),$$

$\sigma \in [0.005, 0.08]$ is an easily tuned parameter. In this way, the pixels in the transition area are treated as mixed pixels. However, there is one vital problem with (8)—this heuristic strategy could only tackle with pixels in the sudden change area. For the vast smooth areas, the mixed information is intractable to achieve. Thus, other strategies are required.

Perhaps, the most direct clue to obtain the guided maps is the intrinsic correlation with the optimal *abundance* \mathbf{A}^* , that is $h_n^* = S(\mathbf{a}_n^*), \forall n \in \{1, 2, \dots, N\}$, where

$$S: \left(\bigcup_{K \geq 1} \mathbb{R}_+^K \right) \rightarrow \mathbb{R}_+$$

is a sparsity measure that maps real vectors to a nonnegative value [62]. Although the optimal *abundance* \mathbf{A}^* is unavailable, the updated *abundance* $\mathbf{A}^{(t)}$ is available after the t^{th} iteration. If $\mathbf{A}^{(t)} \rightarrow \mathbf{A}^*$ over iteration steps, we could always generate a sequence of improved estimates towards the optimal guidance map, that is $\mathbf{h}^{(t)} \rightarrow \mathbf{h}^*$, by using the dependence of $h_n^{(t)} = S(\mathbf{a}_n^{(t)})$, $\mathbf{h}^{(t)} = \left\{ h_n^{(t)} \right\}_{n=1}^N$. In turn, the learnt $\mathbf{h}^{(t)}$ helps to impose an improved individual sparsity constraint for each

pixel, eventually leading to a more reliable unmixing result. This iterative process is supposed to generate a sequence of ever improved estimates until convergences.

Specifically, due to the good property [62], we use the Gini index to measure the sparse level of each *abundance* vector. Given a vector \mathbf{a} with its elements sorted as $a_{(1)} \leq a_{(2)} \leq \dots \leq a_{(K)}$, the Gini index is defined as

$$S(\mathbf{a}) = 1 - 2 \sum_{k=1}^K \frac{a_{(k)}}{\|\mathbf{a}\|_1} \left(\frac{K - k + \frac{1}{2}}{K} \right). \quad (9)$$

In this way, large elements have a smaller weight than the small elements in the sparse measure, avoiding the situation where smaller elements have negligible (or no) effect on the measure of sparsity [62].

C. Robust HU Model via Joint $\ell_{2,1}$ -norm and ℓ_p -norm

Considering the robust representation loss (5) and the pixel-level sparsity constraint (7) together, the overall HU objective (RRLbS) is given by

$$\min_{\mathbf{M} \geq \mathbf{0}, \mathbf{A} \geq \mathbf{0}} \mathcal{O} = \frac{1}{2} \|\mathbf{X} - \mathbf{MA}\|_{2,1} + \lambda \|\mathbf{A}^{1-\mathbf{H}}\|_1, \quad (10)$$

where λ is a nonnegative balancing parameter. Due to the non-convex and non-smooth property of (10), the above objective is very challenging to solve. The efficient solver as well as its convergent proofs and computational complexity analyses will be systematically provided in the next section.

IV. AN EFFICIENT ALGORITHM FOR RRLBS

Since (10) is highly non-convex and non-smooth in \mathbf{M} and \mathbf{A} , the final objective (10) is challenging to solve. As a profound theoretical contribution, we propose an efficient iterative algorithm to solve the joint $\ell_{2,1}$ -norm and ℓ_p -norm based model. We first introduce how to efficiently solve (10) and then give a systematic analysis to the proposed solver, including its convergence and computation complexity.

A. Updating Rules for RRLbS

To ensure the Lipschitz condition [6, 63] of the learning-based sparsity constraint, we reformulate our model as

$$\min_{\mathbf{M} \geq \mathbf{0}, \mathbf{A} \geq \mathbf{0}} \mathcal{O} = \frac{1}{2} \|\mathbf{X} - \mathbf{MA}\|_{2,1} + \lambda \left\| (\mathbf{A} + \xi)^{1-\mathbf{H}} \right\|_1, \quad (11)$$

where ξ is a small positive value adding to every entry in \mathbf{A} . As a result, $A_{kn} + \xi > 0 (\forall k, n)$ guarantees the Lipschitz condition of the learning-based sparsity constraint. It is obvious that (11) is reduced to (10) when $\xi \rightarrow 0$.

Then, the Lagrangian multiplier is used to deal with the nonnegative constraint on \mathbf{M} and \mathbf{A} , resulting in the following objective

$$\min_{\mathbf{M}, \mathbf{A}} \mathcal{L} = \frac{1}{2} \|\mathbf{X} - \mathbf{MA}\|_{2,1} + \lambda \left\| (\mathbf{A} + \xi)^{1-\mathbf{H}} \right\|_1 + \text{Tr}(\Lambda \mathbf{M}^T) + \text{Tr}(\Gamma \mathbf{A}^T), \quad (12)$$

where $\Lambda \in \mathbb{R}_+^{L \times K}$ and $\Gamma \in \mathbb{R}_+^{K \times N}$ are the Lagrangian multipliers of the inequality constraints $\mathbf{M} \geq \mathbf{0}$ and $\mathbf{A} \geq \mathbf{0}$

respectively. There are two variable matrices in (12). Thus, an alternate algorithm is proposed. Specifically, the solution with respect to $\{\mathbf{M}, \mathbf{A}\}$ is given in the following theorem.

Theorem 1. *An updated point $\{\mathbf{M}, \mathbf{A}\}$ could be achieved via the updating rules as*

$$M_{lk} \leftarrow M_{lk} \frac{(\mathbf{UXA}^T)_{lk}}{(\mathbf{UMAA}^T)_{lk}} \quad (13)$$

$$A_{kn} \leftarrow A_{kn} \frac{(\mathbf{M}^T \mathbf{UX})_{kn}}{\left(\mathbf{M}^T \mathbf{UMA} + \lambda (1 - \mathbf{H}) \circ (\mathbf{A} + \xi)^{-\mathbf{H}} \right)_{kn}}, \quad (14)$$

where $\mathbf{U} \in \mathbb{R}_+^{L \times L}$ is a positive-definite and diagonal matrix with the l^{th} diagonal entry³ as $U_{ll} = \frac{1}{2} \left\| (\mathbf{MA} - \mathbf{X})^l \right\|_2^{-1}$; \circ is the Hadamard product between matrices; $\mathbf{A}^{-\mathbf{H}} = \left[A_{kn}^{-H_{kn}} \right]$ is an element-wise exponential operation.

Proof: According to the constrained optimization, a stationary point of (12) could be achieved by differentiating (12), setting the partial derivatives to zero and considering the Karush-Kuhn-Tucker (KKT) optimality conditions [64, 65]. This amounts to a two-step strategy. First, setting the partial derivatives to zero, we have

$$\nabla_{\mathbf{M}} \mathcal{L} = \mathbf{U} (\mathbf{MA} - \mathbf{X}) \mathbf{A}^T + \Lambda = \mathbf{0} \quad (15)$$

$$\begin{aligned} \nabla_{\mathbf{A}} \mathcal{L} &= \mathbf{M}^T \mathbf{U} (\mathbf{MA} - \mathbf{X}) + \Gamma + \\ &\lambda (1 - \mathbf{H}) \circ (\mathbf{A} + \xi)^{-\mathbf{H}} = \mathbf{0}. \end{aligned} \quad (16)$$

Then, considering the KKT conditions $\Lambda_{lk} M_{lk} = 0$ and $\Gamma_{kn} A_{kn} = 0$, we have the equalities as

$$\begin{aligned} (\mathbf{UMAA}^T - \mathbf{UXA}^T)_{lk} M_{lk} &= 0 \\ \left(\mathbf{M}^T \mathbf{U} (\mathbf{MA} - \mathbf{X}) + \lambda (1 - \mathbf{H}) \circ (\mathbf{A} + \xi)^{-\mathbf{H}} \right)_{kn} A_{kn} &= 0. \end{aligned}$$

Solving the above equations, we get the final updating rules

$$\begin{aligned} M_{lk} &\leftarrow M_{lk} \frac{(\mathbf{UXA}^T)_{lk}}{(\mathbf{UMAA}^T)_{lk}} \\ A_{kn} &\leftarrow A_{kn} \frac{(\mathbf{M}^T \mathbf{UX})_{kn}}{\left(\mathbf{M}^T \mathbf{UMA} + \lambda (1 - \mathbf{H}) \circ (\mathbf{A} + \xi)^{-\mathbf{H}} \right)_{kn}}. \end{aligned}$$

In this manner, we give the solver for the objective (11). ■

As mentioned before, the most direct clue to estimate the guidance map \mathbf{h} is the crucial dependence upon *abundances*. Once getting the stable *abundance* \mathbf{A} , \mathbf{h} could be efficiently solved via the Gini index (9) as

$$\mathbf{H} = \mathbf{1}_K \mathbf{h}^T, \mathbf{h} = S(\mathbf{A}). \quad (17)$$

Note that, to satisfy the ℓ_p sparse constraint in (6), every value in the guidance map needs to be scaled into the range of $[0, 0.5]$, that is

$$h_n \leftarrow \frac{h_n - \min(\mathbf{h})}{2 [\max(\mathbf{h}) - \min(\mathbf{h})]}, \quad \forall n \in \{1, 2, \dots, N\}.$$

The solver for the RRLbS model (10) is given in Algorithm 1.

³To avoid singular failures, if $(\mathbf{MA} - \mathbf{X})^l = \mathbf{0}$, we obtain U_{ll} by $U_{ll} = \frac{1}{2} \sqrt{\|(\mathbf{MA} - \mathbf{X})^l\|_2^2 + \epsilon}$, where ϵ is typically set 10^{-8} .

Algorithm 1 for RRLbS (10)

Input: hyperspectral image \mathbf{X} ; the number of *endmembers* K ; parameter λ ; the initial guidance map $\mathbf{h}^{(0)}$.

- 1: initialize the factor matrices \mathbf{M} and \mathbf{A} .
- 2: calculate $\mathbf{H} = \mathbf{1}_K (\mathbf{h}^{(0)})^\top \in \mathbb{R}^{K \times N}$.
- 3: **repeat**
- 4: **repeat**
- 5: update \mathbf{A} via the updating rule (14).
- 6: update \mathbf{M} via the updating rule (13).
- 7: **until** stable
- 8: update \mathbf{H} via the updating rule (17).
- 9: **until** convergence

Output \mathbf{M} and \mathbf{A} as the final unmixing result.

B. Convergence Analysis

To ensure the reliability of (13) and (14), we would like to analyze their convergence property.

Lemma 2. *The updating rules (13) and (14) are equivalent to the following updating rules*

$$\widehat{M}_{lk} \leftarrow \widehat{M}_{lk} \frac{(\widehat{\mathbf{X}}\mathbf{A}^T)_{lk}}{(\widehat{\mathbf{M}}\mathbf{A}\mathbf{A}^T)_{lk}} \quad (18)$$

$$A_{kn} \leftarrow A_{kn} \frac{(\widehat{\mathbf{M}}^T\widehat{\mathbf{X}})_{kn}}{(\widehat{\mathbf{M}}^T\widehat{\mathbf{M}}\mathbf{A} + \lambda(\mathbf{1} - \mathbf{H}) \circ (\mathbf{A} + \xi)^{-\mathbf{H}})_{kn}}, \quad (19)$$

where $\widehat{\mathbf{M}} = \mathbf{U}^{\frac{1}{2}}\mathbf{M}$, $\widehat{\mathbf{X}} = \mathbf{U}^{\frac{1}{2}}\mathbf{X}$. This means that the objective (10) could be equivalently solved by (18) and (19).

Proof: Considering $\widehat{\mathbf{M}} = \mathbf{U}^{\frac{1}{2}}\mathbf{M}$, $\widehat{\mathbf{X}} = \mathbf{U}^{\frac{1}{2}}\mathbf{X}$ and that \mathbf{U} is a positive-definite and diagonal matrix, the updating rules (18) and (19) become

$$U_{ll}^{\frac{1}{2}}M_{lk} \leftarrow U_{ll}^{\frac{1}{2}}M_{lk} \frac{(\mathbf{U}^{\frac{1}{2}}\mathbf{X}\mathbf{A}^T)_{lk}}{(\mathbf{U}^{\frac{1}{2}}\mathbf{M}\mathbf{A}\mathbf{A}^T)_{lk}} \quad (20)$$

$$A_{kn} \leftarrow A_{kn} \frac{(\mathbf{M}^T\mathbf{U}\mathbf{Y})_{kn}}{(\mathbf{M}^T\mathbf{U}\mathbf{M}\mathbf{A} + \lambda(\mathbf{1} - \mathbf{H}) \circ (\mathbf{A} + \xi)^{-\mathbf{H}})_{kn}}. \quad (21)$$

Since $(\mathbf{U}^{\frac{1}{2}}\mathbf{Y})_{lk} = U_{ll}^{\frac{1}{2}}Y_{lk}, \forall \mathbf{Y} \in \mathbb{R}^{L \times K}$, we have the following derivations

$$\frac{(\mathbf{U}^{\frac{1}{2}}\mathbf{X}\mathbf{A}^T)_{lk}}{(\mathbf{U}^{\frac{1}{2}}\mathbf{M}\mathbf{A}\mathbf{A}^T)_{lk}} = \frac{U_{ll}^{\frac{1}{2}}(\mathbf{U}^{\frac{1}{2}}\mathbf{X}\mathbf{A}^T)_{lk}}{U_{ll}^{\frac{1}{2}}(\mathbf{U}^{\frac{1}{2}}\mathbf{M}\mathbf{A}\mathbf{A}^T)_{lk}} = \frac{(\mathbf{U}\mathbf{X}\mathbf{A}^T)_{lk}}{(\mathbf{U}\mathbf{M}\mathbf{A}\mathbf{A}^T)_{lk}}. \quad (22)$$

Substituting (22) into (20), we have

$$M_{lk} \leftarrow M_{lk} \frac{(\mathbf{U}\mathbf{X}\mathbf{A}^T)_{lk}}{(\mathbf{U}\mathbf{M}\mathbf{A}\mathbf{A}^T)_{lk}}. \quad (23)$$

Since the updating rules (23), (21) are exact the same as the updating rules (13), (14), we have proved Lemma 2. ■

Theorem 3. *The objective (10) is non-increasing by using the updating rules (13) and (14).*

Proof: Based on the partial derivatives (15), (16), it is obvious that the updating rules (13), (14) compute the optimal solution of the following problem,

$$\min_{\mathbf{M} \geq \mathbf{0}, \mathbf{A} \geq \mathbf{0}} \frac{1}{2} \text{Tr} \left\{ (\mathbf{X} - \mathbf{M}\mathbf{A})^T \mathbf{U} (\mathbf{X} - \mathbf{M}\mathbf{A}) \right\} + \lambda \left\| (\mathbf{A} + \xi)^{1-\mathbf{H}} \right\|_1 \quad (24)$$

which is equivalent to the objective as:

$$\min_{\widehat{\mathbf{M}} \geq \mathbf{0}, \mathbf{A} \geq \mathbf{0}} \frac{1}{2} \left\| \widehat{\mathbf{X}} - \widehat{\mathbf{M}}\mathbf{A} \right\|_F^2 + \lambda \left\| (\mathbf{A} + \xi)^{1-\mathbf{H}} \right\|_1, \quad (25)$$

where $\widehat{\mathbf{M}} = \mathbf{U}^{\frac{1}{2}}\mathbf{M}$, $\widehat{\mathbf{X}} = \mathbf{U}^{\frac{1}{2}}\mathbf{X}$. It has been proved in [6] that (25) is non-increasing under the updating rules (18), (19). Because (24) is the same problem as (25), and the updating rules (13), (14) are equivalent to (18), (19), as analyzed in Lemma 2, we infer that the objective (24) is non-increasing under the updating rules (13), (14) as well. For each iteration, we denote the updated $\{\mathbf{M}, \mathbf{A}\}$ as $\{\bar{\mathbf{M}}, \bar{\mathbf{A}}\}$. Thus, we have the following inequalities

$$\begin{aligned} & \frac{1}{2} \text{Tr} \{ \bar{\mathbf{E}}^T \mathbf{U} \bar{\mathbf{E}} \} + \lambda \left\| (\bar{\mathbf{A}} + \xi)^{1-\mathbf{H}} \right\|_1 \\ & \leq \frac{1}{2} \text{Tr} \{ \mathbf{E}^T \mathbf{U} \mathbf{E} \} + \lambda \left\| (\mathbf{A} + \xi)^{1-\mathbf{H}} \right\|_1, \end{aligned}$$

where $\bar{\mathbf{E}} = \mathbf{X} - \bar{\mathbf{M}}\bar{\mathbf{A}}$ and $\mathbf{E} = \mathbf{X} - \mathbf{M}\mathbf{A}$. This amounts to

$$\begin{aligned} & \sum_{l=1}^L \frac{\|\bar{\mathbf{e}}^l\|_2^2}{2\|\mathbf{e}^l\|_2} + \lambda \left\| (\bar{\mathbf{A}} + \xi)^{1-\mathbf{H}} \right\|_1 \\ & \leq \sum_{l=1}^L \frac{\|\mathbf{e}^l\|_2^2}{2\|\mathbf{e}^l\|_2} + \lambda \left\| (\mathbf{A} + \xi)^{1-\mathbf{H}} \right\|_1. \end{aligned} \quad (26)$$

Given the function $f(x) = x - \frac{x^2}{2\alpha} (\forall \alpha \in \mathbb{R}_+)$, $f(x) \leq f(\alpha)$ holds for any $x \in \mathbb{R}$ [56, 58]. Thus we have

$$\sum_{l=1}^L \|\mathbf{e}^l\|_2 - \sum_{l=1}^L \frac{\|\bar{\mathbf{e}}^l\|_2^2}{2\|\mathbf{e}^l\|_2} \leq \sum_{l=1}^L \|\mathbf{e}^l\|_2 - \sum_{l=1}^L \frac{\|\mathbf{e}^l\|_2^2}{2\|\mathbf{e}^l\|_2}. \quad (27)$$

Combining the inequalities of (26) and (27) together, we have the inequality as

$$\begin{aligned} & \sum_l \|\bar{\mathbf{e}}^l\|_2 + \lambda \left\| (\bar{\mathbf{A}} + \xi)^{1-\mathbf{H}} \right\|_1 \\ & \leq \sum_l \|\mathbf{e}^l\|_2 + \lambda \left\| (\mathbf{A} + \xi)^{1-\mathbf{H}} \right\|_1, \end{aligned}$$

which is equivalent to the inequality

$$\begin{aligned} & \frac{1}{2} \left\| \mathbf{X} - \bar{\mathbf{M}}\bar{\mathbf{A}} \right\|_{2,1} + \lambda \left\| (\bar{\mathbf{A}} + \xi)^{1-\mathbf{H}} \right\|_1 \\ & \leq \frac{1}{2} \left\| \mathbf{X} - \mathbf{M}\mathbf{A} \right\|_{2,1} + \lambda \left\| (\mathbf{A} + \xi)^{1-\mathbf{H}} \right\|_1. \end{aligned}$$

In this way, we have proven Theorem 3. ■

Apart from the theoretical proof above, the empirical convergence study for Algorithm 1 is summarized in Section V-G.

Table I
COMPUTATIONAL OPERATION COUNTS FOR NMF AND RRLBS AT EACH ITERATION.

| Methods | Arithmetic Operations in float-point format at each iteration | | | | Overall |
|---------|---|-------------------------------|----------|----------|----------|
| | Addition | Multiplication | Division | Exponent | |
| NMF | $2LNK - 2K(N+L) + 2K^2(L+N) - 2K^2$ | $2LNK + K(L+N) + 2K^2(L+N)$ | $K(L+N)$ | - | $O(KLN)$ |
| RRLbS | $3KLN - K(L+N) + 2K^2(L+N) - 2K^2$ | $3KLN + L(3K+N) + K^2(2L+3N)$ | $K(L+N)$ | $KN+L$ | $O(KLN)$ |

Table II
PARAMETERS USED IN COMPUTATIONAL COMPLEXITY ANALYSIS.

| Parameters | Description |
|------------|---|
| K | number of <i>endmembers</i> |
| L | number of channels |
| N | number of pixels in hyperspectral image |
| t | number of iteration steps |

C. Computational Complexity Analysis

Theoretically, the computational complexity is important for algorithms. In this section, we analyze the additional computational cost of our method compared with the standard NMF. To give a precise comparison, the arithmetic operations of addition, multiplication, division and exponent, are counted for each iteration.

Based on the updating rules (13) and (14), it is easy to summarize the counts of operations in Tabel I, where the notations are listed in Table II. For RRLbS, it is important to note that \mathbf{U} is a positive-defined diagonal matrix. This property facilitates the savage of computational costs. For example, it only costs L exponent operations to compute the exponent of $\mathbf{U} \in \mathbb{R}_+^{L \times L}$, that is $\mathbf{U}^\alpha = \{U_{ii}^\alpha\}_{i=1}^L, \forall \alpha \in \mathbb{R}$. While for a normal matrix $\mathbf{V} \in \mathbb{R}_+^{L \times L}$ of the same size, it costs $O(L^3)$ to get the inverse matrix $\mathbf{V}^\alpha (\alpha = -1)$, which could also be treated as an exponent operation. The cost of matrix multiplication $\mathbf{U}\mathbf{M}$ is greatly saved as well; it costs LK multiplication for our case. While for a normal $\mathbf{V} \in \mathbb{R}_+^{L \times L}$, it takes L^2K multiplication and $L^2K - LK$ addition to get $\mathbf{V}\mathbf{M}$.

Apart from the updating costs, RRLbS costs $O(4LN)$ to get the initial guidance map and $O(NK + NK \log K)$ to get an updated one. If the updating process stops after t steps and the learning-based guidance map updates after each q (typically 10) iterations, the total cost of RRLbS is

$$O\left(tKLN + 4LN + \frac{t}{q}(NK + NK \log K)\right).$$

While the total cost of NMF is $O(tKLN)$. Generally $N \gg \max\{L, K\}$, the computational complexities of RRLbS and NMF are of the same magnitude.

V. EVALUATION

In this section, extensive experiments are conducted to evaluate the effectiveness of our method in the HU task.

A. Datasets

Three real hyperspectral datasets are used in the experiments. Their information is listed below. The ground truths are obtained by the method introduced in [18, 19, 66, 67].

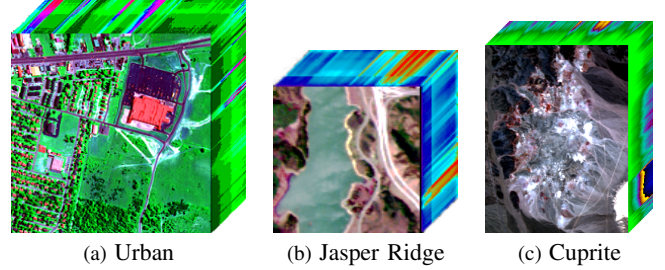


Figure 3. Three benchmark hyperspectral images, that is Urban, Jasper Ridge and Cuprite, used in the experiments.

Urban is one of the most widely used datasets for the HU studying [7, 9, 10]. There are 307×307 pixels. Each pixel is recorded at 210 channels ranging from 400 nm to 2500 nm . Due to the dense water vapor and the atmospheric effects etc., the channels of 1–4, 76, 87, 101–111, 136–153 and 198–210 are either blank or badly noised, which, however, are kept for the unmixing of the hyperspectral image. There are four *endmembers* in this image: “#1 Asphalt”, “#2 Grass”, “#3 Tree” and “#4 Roof” as shown in Fig. 3a.

Jasper Ridge, as shown in Fig. 3b, is a popular dataset used in [61, 68–76]. It consists of 512×614 pixels; each pixel is recorded at 224 channels ranging from 380 nm to 2500 nm , resulting in a very high spectral resolution as 9.46 nm . Since this image is highly complex, we consider a sub-image of 100×100 pixels. This sub-image starts from the (105, 269)-th pixel. Due to dense water vapor and atmospheric effects etc., the channels 1–3, 108–112, 154–166 and 220–224 are blank or badly noised, which, however, are kept for the unmixing process. There are four *endmembers*, that is “#1 Tree”, “#2 Soil”, “#3 Water” and “#4 Road” respectively.

Cuprite (cf. Fig. 3c) is the most benchmark hyperspectral image for the HU research [6, 7, 9, 14, 30, 41, 77–82]. It is captured by the AVIRIS sensor that covers a Cuprite area in Las Vegas, NV, U.S. There are 224 spectral bands that range the spectra from 370 nm to $2,480 \text{ nm}$. The bands 1–2, 104–113, 148–167 and 221–224 are noisy bands or water absorption bands, which are kept for the unmixing process.

In this paper, a subimage of 250×190 pixels is considered, which is widely used in the state-of-the-art HU papers [6, 7, 30, 41]. The researchers have different opinions on the number of endmembers. In [30], there are 14 endmembers; while there are 10 endmembers in [7]; then Dr. Lu hold that there are 12 endmembers in the Cuprite. In this paper, we agree with Dr. Lu’s setting. Please refer to [67] for the illustration of the 12 endmembers. Due to the different setting of endmembers, the results of the state-of-the-art methods are different in the

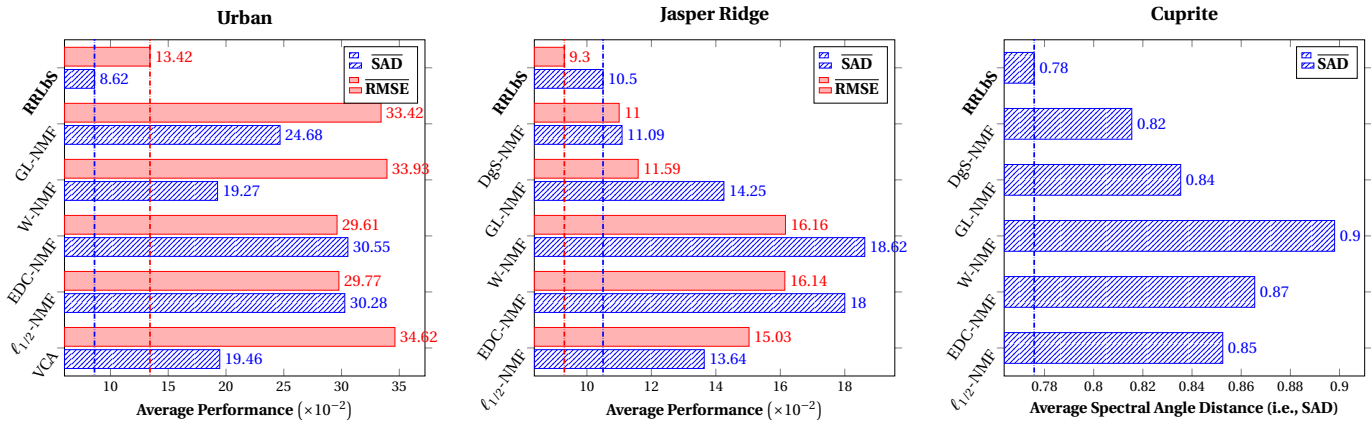


Figure 4. The average performances (i.e. $\overline{\text{SAD}}$ and $\overline{\text{RMSE}}$) of six methods on (a) Urban (b) Jasper Ridge and (c) Cuprite. Compared with the state-of-the-art method, our method achieves highly promising HU results.

papers [7, 9, 14, 30, 41].

B. Compared Algorithms and Parameter Settings

To verify the superior performance, the proposed method is compared with six state-of-the-art methods. The details of all these methods (including our method) are listed as follows:

- 1) **Our method:** Effective Spectral Unmixing via Robust Representation and Learning-based Sparsity (RRLbS) is a new method proposed in this paper.
- 2) Vertex Component Analysis [30] (VCA) is the benchmark geometric method. The code is available on the webpage <http://www.lx.it.pt/biucas/code.htm>.
- 3) $\ell_{1/2}$ sparsity-constrained NMF [7] ($\ell_{1/2}$ -NMF) is a state-of-the-art method that could get sparser results than ℓ_1 -NMF. Since the code is unavailable, we implement it.
- 4) Local Neighborhood Weights regularized NMF [11] (W-NMF) is a manifold graph based NMF method. It integrates the spectral information and spatial information when constructing the weighted graph. Since this work is an extension of G-NMF [12], we implement the code by referring to the code on <http://www.cad.zju.edu.cn/home/dengcai/Data/GNMF.html>.
- 5) *Endmember* Dissimilarity Constrained NMF [14] (EDC-NMF) urges the *endmember* to be smooth itself and different from each other. We implement the code since the original code is not available on the web.
- 6) Graph-regularized $\ell_{1/2}$ -NMF [41] (GL-NMF) is a new method proposed in 2013. It considers both the sparse characteristic and the intrinsic manifold structure in hyperspectral images. We implement the code by ourself.
- 7) Data-guided sparsity constrained NMF [6] (DgS-NMF) is a state-of-the-art method published in 2014. The main idea is to apply the adaptively sparse constraints, which are according to the mixed level of each pixel.

There is no parameter in VCA. For the other six methods, there is one main parameter. To find a good parameter setting, typical procedures consist of two phases: a bracketing phase that finds an interval $[\lambda_{\min}, \lambda_{\max}]$ containing acceptable parameters, and a selection phase that zooms in to locate the optimal parameter.

C. Evaluation Metrics for Quantitative Performances

We use two benchmark metrics to measure the quantitative HU results, i.e. (a) Spectral Angle Distance (SAD) [9, 30] and (b) Root Mean Square Error (RMSE) [7, 9, 83]. Both metrics assess the estimated errors. Thus, the smaller SAD and RMSE correspond to the better results. Specifically, SAD evaluates the estimated *endmember*, and RMSE assesses the estimated *abundance* map. They are defined as

$$\text{SAD}(\mathbf{m}_k, \hat{\mathbf{m}}_k) = \arccos\left(\frac{\mathbf{m}_k^T \hat{\mathbf{m}}_k}{\|\mathbf{m}_k\| \cdot \|\hat{\mathbf{m}}_k\|}\right) \quad (28)$$

and

$$\text{RMSE}(\mathbf{a}^k, \hat{\mathbf{a}}^k) = \left(\frac{1}{N} \|\mathbf{a}^k - \hat{\mathbf{a}}^k\|_2^2\right)^{1/2} \quad (29)$$

$\forall k = \{1, \dots, K\}$, where $\hat{\mathbf{m}}_k$ is the k^{th} estimated *endmember*, $\hat{\mathbf{a}}^k$ is the k^{th} estimated *abundance* map (i.e. the k^{th} row vector in $\hat{\mathbf{A}}$), $\{\mathbf{m}_k, \mathbf{a}^k\}$ are the corresponding ground truth; N is the number of pixels in image.

D. Quantitative Performance Comparisons

To verify the performance of our method, we conduct the experiments on three benchmark datasets, i.e., Urban, Jasper Ridge and Cuprite, as shown in Fig. 3. Each experiment is repeated eight times to ensure a reliable comparison.

The quantitative results are summarized in Tables III, IV, V and plotted in Fig. 4. Specifically, Table III summarizes the unmixing results on Urban, where the top sub-table illustrates SADs and the bottom sub-table shows RMSEs. In each sub-table, each row shows the results of one *endmembers*, i.e. “#1 Tree”, “#2 Soil”, “#3 Water” and “#4 Road” respectively; the last row shows the average results over the four *endmembers*. As Table III shows, our method generally achieves the best results. This case is better illustrated in Fig. 4a, where the average results are illustrated. As we shall see, RRLbS performs the best—compared with the second best results, our method reduces 55.27% for $\overline{\text{SAD}}$ and 54.68% for $\overline{\text{RMSE}}$. Such extraordinary improvements rely on two reasons. First, due to the atmospheric effects, there are 48 channels either blank or badly noised. Accordingly, our method is robust

Table III

UNMIXING PERFORMANCES OF SEVEN STATE-OF-THE-ART METHODS ON URBAN. THE RED VALUE IS THE BEST, AND THE BLUE VALUE IS THE 2ND BEST.

| End-members | Spectral Angle Distance SAD ($\times 10^{-2}$) | | | | | | |
|--|--|-------------------|------------|------------|------------|------------|------------|
| | VCA | $\ell_{1/2}$ -NMF | EDC-NMF | W-NMF | GL-NMF | DgS-NMF | RRLbS |
| #1 Asphalt | 12.22±3.63 | 24.92±0.31 | 17.39±0.41 | 16.10±0.47 | 24.16±0.71 | 29.58±0.83 | 17.35±0.18 |
| #2 Grass | 42.09±6.93 | 29.26±0.11 | 43.48±0.06 | 43.67±0.07 | 30.45±0.08 | 32.64±0.10 | 8.01±0.07 |
| #3 Tree | 12.58±1.04 | 7.45±0.06 | 9.78±0.11 | 11.94±0.23 | 9.77±0.53 | 6.94±0.04 | 3.74±0.06 |
| #4 Roof | 43.81±17.65 | 16.19±0.23 | 50.45±0.22 | 50.49±0.28 | 12.71±0.20 | 29.56±0.61 | 5.38±0.06 |
| Avg. | 27.68 | 19.46 | 30.28 | 30.55 | 19.27 | 24.68 | 8.62 |
| Root Mean Square Error RMSE ($\times 10^{-2}$) | | | | | | | |
| #1 Asphalt | 32.60±1.93 | 29.76± 0.12 | 24.12±0.12 | 23.84±0.12 | 29.19±0.17 | 30.18±0.12 | 10.34±0.05 |
| #2 Grass | 39.78±3.39 | 42.12±0.05 | 34.78±0.07 | 34.34±0.07 | 41.58±0.07 | 41.73±0.10 | 18.23±0.09 |
| #3 Tree | 33.05±5.09 | 40.73±0.03 | 38.82±0.01 | 38.63±0.02 | 40.27±0.02 | 40.72±0.05 | 13.90±0.10 |
| #4 Roof | 33.01±5.61 | 25.86±0.39 | 21.36±0.15 | 21.63±0.17 | 24.69±0.59 | 21.07±0.30 | 11.20±0.10 |
| Avg. | 34.61 | 34.62 | 29.77 | 29.61 | 33.93 | 33.42 | 13.42 |

Table IV

UNMIXING PERFORMANCES OF SEVEN METHODS ON JASPER RIDGE. THE RED VALUE IS THE BEST, AND THE BLUE VALUE IS THE 2ND BEST.

| End-members | Spectral Angle Distance SAD ($\times 10^{-2}$) | | | | | | |
|--|--|-------------------|-------------|------------|------------|------------|------------|
| | VCA | $\ell_{1/2}$ -NMF | EDC-NMF | W-NMF | GL-NMF | DgS-NMF | RRLbS |
| #1 Tree | 24.71±5.83 | 11.66±0.14 | 18.21±0.06 | 18.71±0.09 | 9.71±0.32 | 9.76±0.08 | 8.71±0.13 |
| #2 Soil | 24.72±0.33 | 18.22±0.35 | 21.83± 0.44 | 22.12±0.42 | 10.23±0.09 | 12.34±0.08 | 9.79±0.14 |
| #3 Water | 23.68±14.66 | 3.58±1.02 | 8.51±0.53 | 9.99±0.44 | 20.27±0.63 | 6.25±0.27 | 5.37±0.38 |
| #4 Road | 52.26±6.93 | 21.12±0.11 | 23.44±0.22 | 23.66±0.29 | 16.80±0.29 | 15.98±0.22 | 18.13±0.17 |
| Avg. | 31.34 | 13.64 | 18.00 | 18.62 | 14.25 | 11.09 | 10.50 |
| Root Mean Square Error RMSE ($\times 10^{-2}$) | | | | | | | |
| #1 Tree | 29.05±5.90 | 8.23±0.28 | 13.32±0.13 | 13.73±0.07 | 6.57±0.15 | 7.76±0.23 | 7.04±0.36 |
| #2 Soil | 28.26±9.27 | 6.49±0.02 | 9.39±0.08 | 10.22±0.06 | 6.12±0.03 | 6.47±0.03 | 5.66±0.04 |
| #3 Water | 25.37±7.85 | 22.88±0.28 | 21.32±0.23 | 20.89±0.28 | 17.73±0.61 | 15.73±0.31 | 13.53±0.32 |
| #4 Road | 24.12±16.81 | 22.52±0.47 | 20.54±0.34 | 19.82±0.44 | 15.94±0.65 | 14.06±0.36 | 10.98±0.33 |
| Avg. | 26.70 | 15.03 | 16.14 | 16.16 | 11.59 | 11.00 | 9.30 |

Table V

UNMIXING PERFORMANCE OF SIX STATE-OF-THE-ART METHODS ON CUPRITE. THE RED VALUE IS THE BEST, AND THE BLUE VALUE IS THE 2ND BEST.

| Endmembers | Spectral Angle Distance (SAD) | | | | | |
|---------------------------|-------------------------------|---------------|---------------|---------------|---------------|---------------|
| | $\ell_{1/2}$ -NMF | EDC-NMF | W-NMF | GL-NMF | DgS-NMF | RRLbS |
| #1 Alunite | 0.3378±0.2846 | 0.3274±0.0085 | 1.3462±0.0162 | 0.3176±0.0362 | 0.3000±0.0876 | 0.3120±0.0450 |
| #2 Andradite | 1.3552±0.0355 | 1.5106±0.1238 | 1.3972±0.0474 | 0.8033±0.0305 | 0.8797±0.0516 | 1.4097±0.0413 |
| #3 Buddingtonite | 1.3189±0.0350 | 1.3566±0.0617 | 1.4359±0.0394 | 1.3863±0.0970 | 1.3497±0.0635 | 1.2886±0.0741 |
| #4 Dumortierite | 0.6131±0.1236 | 0.6813±0.4101 | 1.1769±0.0759 | 1.0918±0.3249 | 0.4060±0.1326 | 0.3342±0.0851 |
| #5 Kaolinite ₁ | 0.4148±0.3163 | 0.3300±0.3841 | 1.3173±0.3309 | 0.7197±0.3104 | 1.2451±0.4480 | 0.4651±0.4010 |
| #6 Kaolinite ₂ | 0.3216±0.1869 | 0.4076±0.3442 | 0.3097±0.0567 | 0.3631±0.4211 | 0.3206±0.0081 | 0.2861±0.3214 |
| #7 Muscovite | 1.4228±0.0226 | 1.3684±0.0328 | 1.4419±0.0263 | 1.4412±0.0214 | 1.4152±0.1141 | 1.0391±0.0665 |
| #8 Montmorillonite | 1.1161±0.4560 | 1.1617±0.3705 | 0.3336±0.4429 | 1.4234±0.3953 | 1.1804±0.4017 | 0.3479±0.4526 |
| #9 Nontronite | 0.2892±0.0044 | 0.3103±0.0312 | 0.3024±0.0136 | 0.2896±0.0100 | 0.3030±0.0123 | 0.2825±0.0182 |
| #10 Pyrope | 1.2089±0.3985 | 1.3712±0.1130 | 0.9347±0.3493 | 0.3543±0.3791 | 0.5711±0.0643 | 1.2644±0.3729 |
| #11 Sphene | 0.3998±0.4201 | 1.1496±0.3551 | 0.4702±0.2028 | 0.3805±0.1989 | 0.3614±0.1437 | 0.8332±0.3182 |
| #12 Chalcedony | 1.4315±0.1222 | 0.4117±0.0607 | 0.3105±0.0389 | 1.4540±0.5391 | 1.4538±0.4531 | 1.4468±0.4611 |
| Avg. | 0.8525 | 0.8655 | 0.8980 | 0.8354 | 0.8155 | 0.7758 |

to these side channels and relieves their bad effects on the unmixing process. Besides, with the help of the guidance map, RRLbS exploits an individually sparse constraint according to the mixed level of each pixel, which is better suited to the real situation. Both reasons help to achieve a better performance.

In Table IV, there are two sub-tables illustrating SADs and RMSEs of seven state-of-the-art methods on the Jasper Ridge hyperspectral image. In the sub-table, each row shows the results of one *endmembers*, that is “#1 Tree”, “#2 Soil”, “#3 Water” and “#4 Road” respectively. The last row shows the average results. Specifically, the values in the red ink are the best, while the blue ones are the second best. As Table IV shows, our method generally achieves the best results, and in a few cases it achieves comparable results with the best results of other methods. Such case is better illustrated in Fig. 4b. As

we shall see, RRLbS is the best method that reduces 5.32% for SAD and 15.45% for RMSE according to the second best results. However, compared with the results on Urban, the improvement of our method is not so huge. This is since Jasper Ridge is not so badly noised as Urban. The improvement mainly relies on the individually sparse constraint in RRLbS.

Table V summaries the HU performances of six methods on the Cuprite hyperspectral image. In this table, the rows display the results of 12 *endmembers*, as shown in Table V. In general, the sparsity constrained methods, such as $\ell_{1/2}$ -NMF, GL-NMF and DgS-NMF, obtain better results than the other methods. This is since sparsity constraints tends to achieve expressive *endmembers* [45]. Such property is more reliable for the HU task. In Fig. 4c, the average performances of SAD are exhibited. As we shall see, our method obtains superior

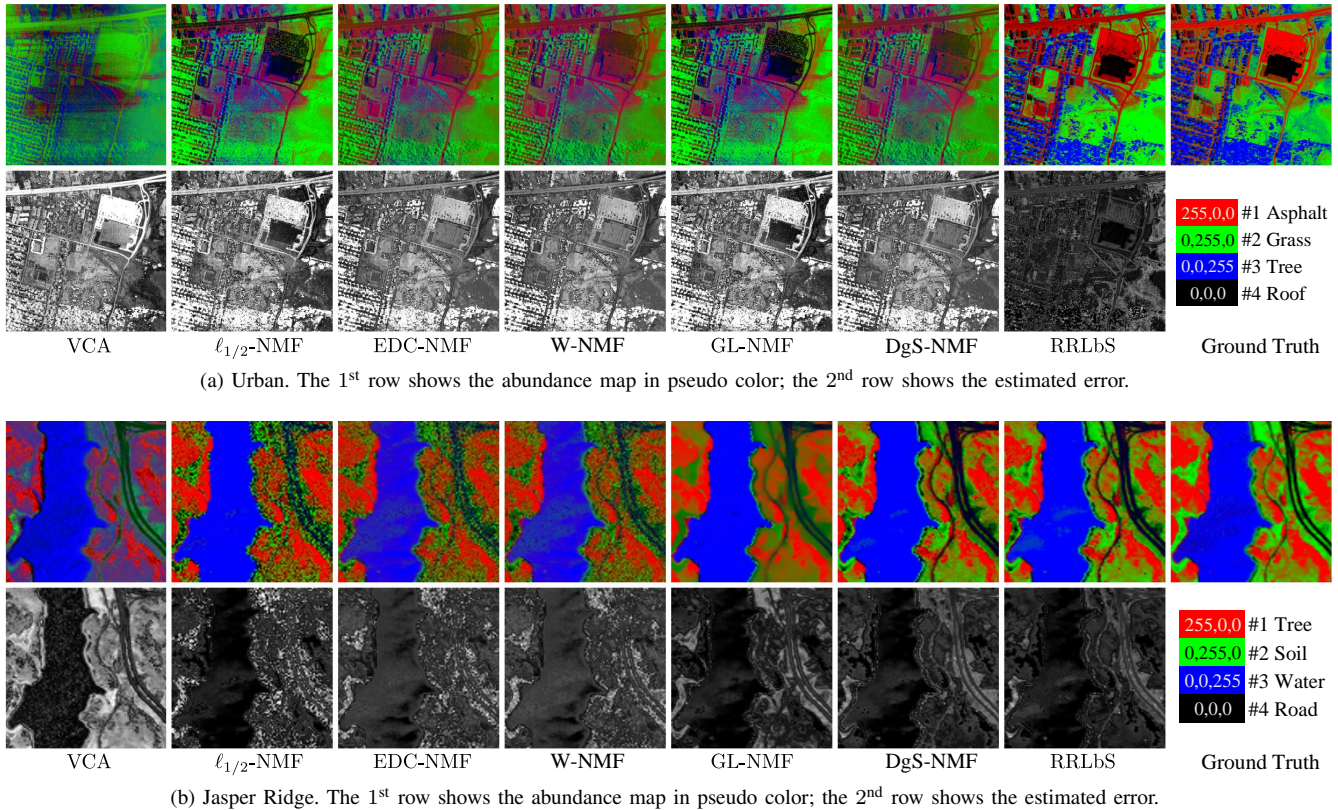


Figure 5. *Abundance* maps of five methods on (a) Urban and (b) Jasper Ridge. In each sub-figure, the top row shows *abundance* maps in pseudo color; the bottom row shows the estimated error of each method, i.e. $\mathbf{e} = \{e_n\}_{n=1}^N$, where $e_n = \|\mathbf{a}_n - \hat{\mathbf{a}}_n\|$. From the 1st to the 5th column, each column illustrates the results of one method. The last column shows the ground truths. (Best viewed in color)

performances—compared with the second best results, RRLbS reduces 4.87% for $\overline{\text{SAD}}$. Cuprite is the most challenging real hyperspectral images. Such improvement is considerable.

E. Visual Performance Comparisons

To give a visible comparison, the *abundance* map of seven methods as well as their estimated errors are compared in Fig. 5. To begin, we give the definition of *abundance* maps in pseudo by taking Fig. 5a as an example. There are four main color inks in the top row of Fig. 5a. Via these colors, we could display the *abundances* A_{kn} associated with pixel \mathbf{x}_n by plotting the corresponding pixel using the proportions of red, blue, green and black inks given by A_{kn} for $k=1, 2, 3, 4$, respectively. So, for instance, a pixel for which $A_{2n}=1$ will be colored blue, whereas one for which $A_{2n}=A_{1n}=0.5$ will be colored with equal proportions of red and blue inks and so will appear purple. In the bottom row of Fig. 5a, the error map $\mathbf{e} = \{e_n\}_{n=1}^N \in \mathbb{R}_+$ is displayed. At the n^{th} pixel, the error value in \mathbf{e} is obtained by computing the ℓ_2 -norm of the corresponding error vector, that is $e_n = \|\mathbf{a}_n - \hat{\mathbf{a}}_n\|_2$.

The visualized *abundances* on the Urban hyperspectral image are illustrated in Fig. 5a, consisting of two rows and eight columns of sub-images. The top row shows the *abundance* map in pseudo, and the bottom rows shows the corresponding error maps. From the 1st to the 7th columns, each column shows the result sub-image of one method. The last column shows the ground truth. As we shall see, our method achieves

extraordinarily results. It gets the most similar *abundance* maps compared with the ground truth; our error map is the smallest. For the other methods, they achieve *abundance* maps that have more errors, which are clearly demonstrated in the corresponding error map. As mentioned before, it is the serious noise in Urban makes other results bad. While for our method, the robust objective could greatly relieve the side effects of outlier channels. Thus, the performance is largely enhanced.

The *abundance* maps of seven state-of-the-art methods on the Jasper Ridge image are displayed in Figs. 5b. Compared with Fig. 5a, most methods achieve acceptable results. This is due to the less noise in the Jasper Ridge image. Specifically, our method achieves much better results than the other methods—our *abundance* map is highly similar with the ground truth; the corresponding error map is very small. Such results verify that the individually sparse constraint is very reliable, and that RRLbS is well suited to the HU task.

F. Comparison of Guidance Maps: Quantitative & Visual

As a significant characteristic, RRLbS learns the guided map to model the individually mixed level of each pixel. Based on the learnt guided map, we impose the individually sparse constraint according to the mixed level of each pixel. These two phases help each other to achieve better and better results. The unmixing results have already been compared. In this section, the learnt guided maps are systematically compared.

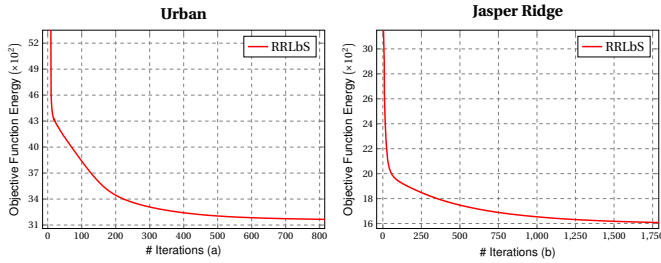


Figure 6. Convergence curves of RRLbS on (a) Urban and (b) Jasper Ridge.

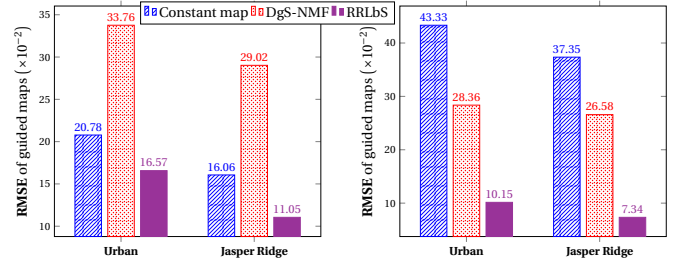
The results of the guided maps are illustrated in Figs. 7a and 7b, where the former summarizes the quantitative results and the latter shows the visual comparisons. There are three kinds of guided maps in Fig. 7: 1) “Constant map” means the identical guided map used by the traditional methods, like, ℓ_1 -NMF and $\ell_{1/2}$ -NMF [6]; 2) “DgS-NMF” denotes the guided learnt by the heuristic strategy in [6]; 3) “RRLbS” represents the learning-based guided map obtained by our RRLbS. As shown in Fig. 7, “RRLbS” is extraordinarily better than the other two methods. In terms of quantitative comparisons (cf. Fig. 7a), the estimated error of “RRLbS” is half of the second best one in average. When checking the visual comparison in Figs. 7b, our method achieves the most similar appearance compared with the ground truth. Obviously, there is no meaning for the “Constant map”. For the “DgS-NMF”, it achieves acceptable results in the transitional areas in the scene. However, it is intractable to guess the mixed information for the vast smooth areas. As a huge improvement, the “RRLbS” gets satisfactory mixed information in all kinds of areas. In short, the comparisons above verify that RRLbS is able to learn satisfactory guidance maps which can effectively indicate the mixed level of pixels.

G. Convergence Study

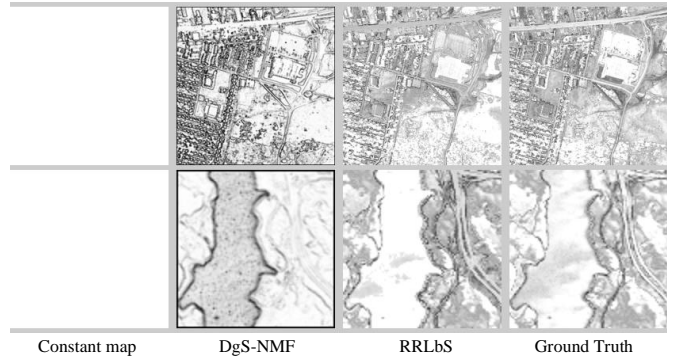
It has been theoretically proven that the objective (10) is able to converge to a local minimum by using the updating rules (13) and (14). To verify this conclusion, we conduct experiments to show the empirical convergence property of RRLbS. The convergent curves are illustrated in Fig. 6, including two sub-figures, each of which shows the results on one dataset. In each sub-figure, the X-axis shows the number of iteration t , and the Y-axis illustrates the objective energy defined in (10). As we shall see, the objective energy decreases monotonously over the iteration steps until convergence.

VI. CONCLUSIONS

In this paper, we propose a novel robust representation and learning-based sparsity (RRLbS) based method for the HU task. The $\ell_{2,1}$ -norm is exploited to measure the representation loss, enhancing the robustness against outlier channels. Then, through the learning-based sparsity method, the sparse constraint is adaptively applied according to the mixed level of each pixel. Such case not only agrees with the practical situation but also leads the *endmember* toward some spectra



(a) Quantitative results of the three guided maps on Urban and Jasper Ridge.



(b) Visual results of the three guided maps on Urban and Jasper Ridge.

Figure 7. Illustrations of three guided maps on the two datasets: (a) quantitative results, (b) visual results. Specifically, “Constant map” means the identical guided map used in the traditional methods, e.g., ℓ_1 -NMF and $\ell_{1/2}$ -NMF; “DgS-NMF” denotes the guided map obtained by the heuristic strategy in [6]; “RRLbS” represents the learning-based guided map achieved by the proposed method. (a) shows the SAD and RMSE error of those three methods compared with the ground truths. In (b), there are two rows and four columns of sub-images. Each row shows the results on one dataset, i.e. Urban and Jasper Ridge respectively. From the 1st to the 3rd column, each column illustrates the results of one method. The last column shows the ground truths.

resembling the highly sparse regularized pixel. Extensive experiments on three benchmark datasets verify the advantages of RRLbS: 1) in terms of both quantitative and visual performances, RRLbS achieves extraordinarily better results than all the compared methods; 2) the estimated guidance map is highly promising as well, providing a more accurate sparse constraint at the pixel level. Moreover, both theoretic proof and empirical results verify the convergence of our method.

APPENDIX

In this appendix, we will provide a $\ell_{2,p}$ -norm based robust model to deal with the badly degraded channel. Specifically in Section III-C, we have proposed the $\ell_{2,1}$ -norm based measure for the representation error, leading to the following objective

$$\min_{\mathbf{M} \geq 0, \mathbf{A} \geq 0} \mathcal{O} = \frac{1}{2} \|\mathbf{X} - \mathbf{MA}\|_{2,1} + \lambda \|\mathbf{A}^{1-\mathbf{H}}\|_1. \quad (30)$$

However, there are theoretical and empirical evidences to demonstrate the fact that compared with ℓ_2 or ℓ_1 norms, the ℓ_p ($0 < p < 1$)-norm is more able to prevent outliers from dominating the objective, enhancing the robustness [84]. Therefore, we provide another new model by using the $\ell_{2,p}$ ($0 < p < 1$)-norm to measure the representation loss

$$\min_{\mathbf{M} \geq 0, \mathbf{A} \geq 0} \mathcal{O} = \frac{1}{2} \|\mathbf{X} - \mathbf{MA}\|_{2,p} + \lambda \|\mathbf{A}^{1-\mathbf{H}}\|_1, \quad (31)$$

where $\|\mathbf{X} - \mathbf{MA}\|_{2,p} = \sum_l^L \left(\sum_n^N (\mathbf{X} - \mathbf{MA})_{ln}^2 \right)^{p/2}$. In this case, we could control the robustness level of our model (31) by setting the value of p —a smaller p leads to a strong robustness under the same λ setting.

REFERENCES

- [1] K. C. Mertens, L. P. C. Verbeke, E. I. Ducheyne, and R. R. D. Wulf, "Using genetic algorithms in sub-pixel mapping," *International Journal of Remote Sensing (IJRS)*, vol. 24, no. 21, pp. 4241–4247, 2003.
- [2] R. Kawakami, J. Wright, Y.-W. Tai, Y. Matsushita, M. Ben-Ezra, and K. Ikeuchi, "High-resolution hyperspectral imaging via matrix factorization," *IEEE Conference on Computer Vision and Pattern Recognition (CVPR)*, vol. 0, pp. 2329–2336, 2011.
- [3] Z. Guo, T. Wittman, and S. Osher, "L1 unmixing and its application to hyperspectral image enhancement," in *Defense, Security, and Sensing*, ser. Society of Photo-Optical Instrumentation Engineers (SPIE) Conference Series, vol. 7334, no. 1. The International Society for Optical Engineering., Apr. 2009, p. 73341M.
- [4] C. Li, T. Sun, K. Kelly, and Y. Zhang, "A compressive sensing and unmixing scheme for hyperspectral data processing," *IEEE Transactions on Image Processing (TIP)*, vol. 21, no. 3, pp. 1200–1210, March 2012.
- [5] S. Cai, Q. Du, and R. Moorhead, "Hyperspectral imagery visualization using double layers," *IEEE Transactions on Geoscience and Remote Sensing (TGRS)*, vol. 45, no. 10, pp. 3028–3036, Oct 2007.
- [6] F. Zhu, Y. Wang, B. Fan, S. Xiang, G. Meng, and C. Pan, "Spectral unmixing via data-guided sparsity," *IEEE Transactions on Image Processing (TIP)*, vol. 23, no. 12, pp. 5412–5427, Dec 2014.
- [7] Y. Qian, S. Jia, J. Zhou, and A. Robles-Kelly, "Hyperspectral unmixing via sparsity-constrained nonnegative matrix factorization," *IEEE Transactions on Geoscience and Remote Sensing (TGRS)*, vol. 49, no. 11, pp. 4282–4297, nov 2011.
- [8] H. Li, Y. Wang, S. Xiang, J. Duan, F. Zhu, and C. Pan, "A label propagation method using spatial-spectral consistency for hyperspectral image classification," *International Journal of Remote Sensing*, vol. 37, no. 1, pp. 191–211, 2016.
- [9] X. Liu, W. Xia, B. Wang, and L. Zhang, "An approach based on constrained nonnegative matrix factorization to unmix hyperspectral data," *IEEE Transactions on Geoscience and Remote Sensing (TGRS)*, vol. 49, no. 2, pp. 757–772, 2011.
- [10] S. Jia and Y. Qian, "Constrained nonnegative matrix factorization for hyperspectral unmixing," *IEEE Transactions on Geoscience and Remote Sensing (TGRS)*, vol. 47, no. 1, pp. 161–173, 2009.
- [11] J. Liu, J. Zhang, Y. Gao, C. Zhang, and Z. Li, "Enhancing spectral unmixing by local neighborhood weights," *IEEE Journal of Selected Topics in Applied Earth Observations and Remote Sensing*, vol. 5, no. 5, pp. 1545–1552, 2012.
- [12] D. Cai, X. He, J. Han, and T. S. Huang, "Graph regularized nonnegative matrix factorization for data representation," *IEEE Transactions on Pattern Analysis and Machine Intelligence (PAMI)*, vol. 33, no. 8, pp. 1548–1560, aug 2011.
- [13] L. Miao, H. Qi, and H. Qi, "Endmember extraction from highly mixed data using minimum volume constrained nonnegative matrix factorization," *IEEE Transactions on Geoscience and Remote Sensing (TGRS)*, vol. 45, no. 3, pp. 765–777, 2007.
- [14] N. Wang, B. Du, and L. Zhang, "An endmember dissimilarity constrained non-negative matrix factorization method for hyperspectral unmixing," *IEEE Journal of Selected Topics in Applied Earth Observations and Remote Sensing*, vol. 6, no. 2, pp. 554–569, 2013.
- [15] M.-D. Iordache, J. M. Bioucas-Dias, and A. Plaza, "Sparse unmixing of hyperspectral data," *IEEE Transactions Geoscience and Remote Sensing (TGRS)*, vol. 49, no. 6, pp. 2014–2039, 2011.
- [16] M.-D. Iordache, J. Bioucas-Dias, and A. Plaza, "Total variation spatial regularization for sparse hyperspectral unmixing," *IEEE Transactions on Geoscience and Remote Sensing (TGRS)*, vol. 50, no. 11, pp. 4484–4502, 2012.
- [17] J. Bayliss, J. A. Gualtieri, and R. F. Cromp, "Analyzing hyperspectral data with independent component analysis," in *Proc. SPIE*, vol. 3240. SPIE, 1997, pp. 133–143.
- [18] S. Jia and Y. Qian, "Spectral and spatial complexity-based hyperspectral unmixing," *IEEE Transactions on Geoscience and Remote Sensing (TGRS)*, vol. 45, no. 12, pp. 3867–3879, 2007.
- [19] F. Zhu, Y. Wang, S. Xiang, B. Fan, and C. Pan, "Structured sparse method for hyperspectral unmixing," *ISPRS Journal of Photogrammetry and Remote Sensing*, vol. 88, pp. 101–118, 2014.
- [20] G. Cheng, Y. Wang, Y. Gong, F. Zhu, and C. Pan, "Urban road extraction via graph cuts based probability propagation," in *Image Processing (ICIP), 2014 IEEE International Conference on*. IEEE, 2014, pp. 5072–5076.
- [21] J. Yao, X. Zhu, F. Zhu, and J. Huang, "Deep correlational learning for survival prediction from multi-modality datay," in *International Conference on Medical Image Computing and Computer Assisted Intervention (MICCAI)*, 2017.
- [22] G. Cheng, Y. Wang, F. Zhu, and C. Pan, "Road extraction via adaptive graph cuts with multiple features," in *Image Processing (ICIP), IEEE International Conference on*. IEEE, 2015, pp. 3962–3966.
- [23] X. Hu, Y. Wang, F. Zhu, and C. Pan, "Learning-based fully 3d face reconstruction from a single image," in *Acoustics, Speech and Signal Processing (ICASSP), 2016 IEEE International Conference on*. IEEE, 2016, pp. 1651–1655.
- [24] Z. Xu, S. Wang, F. Zhu, and J. Huang, "Seq2seq fingerprint: An unsupervised deep molecular embedding for drug discovery," in *ACM Conference on Bioinformatics, Computational Biology, and Health Informatics (ACM-BCB)*, 2017.
- [25] G. Cheng, F. Zhu, S. Xiang, Y. Wang, and C. Pan, "Accurate urban road centerline extraction from vhr imagery via multiscale segmentation and tensor voting," *Neurocomputing*, vol. 205, pp. 407–420, 2016.
- [26] X. Zhu, J. Yao, F. Zhu, and J. Huang, "Wsis: Making survival prediction from whole slide histopathological images," in *IEEE Conference on Computer Vision and Pattern Recognition*, 2017, pp. 7234 – 7242.
- [27] G. Cheng, F. Zhu, S. Xiang, and C. Pan, "Road centerline extraction via semisupervised segmentation and multidirection nonmaximum suppression," *IEEE Geoscience and Remote Sensing Letters*, vol. 13, no. 4, pp. 545–549, 2016.
- [28] F. Zhu and P. Liao, "Effective warm start for the online actor-critic reinforcement learning based mhealth intervention," in *The Multi-disciplinary Conference on Reinforcement Learning and Decision Making*, 2017, pp. 6 – 10.
- [29] J. M. Boardman, F. A. Kruse, and R. O. Green, "Mapping target signatures via partial unmixing of aviris data," in *Proc. Summ. JPL Airborne Earth Sci. Workshop*, vol. 1, 1995, p. 23–26.
- [30] J. M. P. Nascimento and J. M. B. Dias, "Vertex component analysis: a fast algorithm to unmix hyperspectral data," *IEEE Transactions on Geoscience and Remote Sensing (TGRS)*, vol. 43, no. 4, pp. 898–910, 2005.
- [31] C.-I. Chang, C.-C. Wu, W. Liu, and Y. C. Ouyang, "A new growing method for simplex-based endmember extraction algorithm," *IEEE Transactions on Geoscience and Remote Sensing (TGRS)*, vol. 44, no. 10, pp. 2804–2819, 2006.
- [32] J. Li and J. M. Bioucas-Dias, "Minimum volume simplex analysis: A fast algorithm to unmix hyperspectral data," in *IEEE Geoscience and Remote Sensing Symposium*, vol. 4, 2008, pp. III–250–III–253.
- [33] J. Bioucas-Dias, "A variable splitting augmented lagrangian approach to linear spectral unmixing," in *Workshop on Hyperspectral Image and Signal Processing: Evolution in Remote Sensing*, Aug 2009, pp. 1–4.
- [34] G. Martin and A. Plaza, "Spatial-spectral preprocessing prior to end-member identification and unmixing of remotely sensed hyperspectral data," *IEEE Journal of Selected Topics in Applied Earth Observations and Remote Sensing*, vol. 5, no. 2, pp. 380–395, 2012.
- [35] J. Wang and C.-I. Chang, "Applications of independent component analysis in endmember extraction and abundance quantification for hyperspectral imagery," *IEEE Transactions on Geoscience and Remote Sensing (TGRS)*, vol. 44, no. 9, pp. 2601–2616, 2006.
- [36] N. Dobigeon, S. Moussaoui, M. Coulon, J.-Y. Tourneret, and A. O. Hero, "Joint bayesian endmember extraction and linear unmixing for hyperspectral imagery," *IEEE Transactions on Signal Process (TSP)*, vol. 57, no. 11, pp. 4355–4368, 2009.
- [37] J. M. Bioucas-Dias, "A variable splitting augmented lagrangian approach to linear spectral unmixing," in *Workshop on Hyperspectral Image and Signal Processing: Evolution in Remote Sensing*, 2009, pp. 1–4.
- [38] J. M. P. Nascimento and J. M. Bioucas-Dias, "Hyperspectral unmixing based on mixtures of dirichlet components," *IEEE Transactions on Geoscience and Remote Sensing (TGRS)*, vol. 50, no. 3, pp. 863–878, 2012.
- [39] N. Yokoya, J. Chanussot, and A. Iwasaki, "Nonlinear unmixing of hyperspectral data using semi-nonnegative matrix factorization," *IEEE Transactions on Geoscience and Remote Sensing (TGRS)*, vol. 52, no. 2, pp. 1430–1437, 2014.
- [40] M. E. Winter, "N-findr: an algorithm for fast autonomous spectral end-member determination in hyperspectral data," in *SPIE Conference Imaging Spectrometry*, 1999, pp. 266–275.
- [41] X. Lu, H. Wu, Y. Yuan, P. Yan, and X. Li, "Manifold regularized sparse

- nmf for hyperspectral unmixing,” *IEEE Transactions on Geoscience and Remote Sensing (TGRS)*, vol. 51, no. 5, pp. 2815–2826, 2013.
- [42] D. D. Lee and H. S. Seung, “Learning the parts of objects with nonnegative matrix factorization,” *Nature*, vol. 401, no. 6755, pp. 788–791, Oct 1999.
- [43] S. E. Palmer, “Hierarchical structure in perceptual representation,” *Elsevier Journal of Cognitive Psychology*, vol. 9, no. 4, pp. 441–474, 1977.
- [44] N. K. Logothetis and D. L. Sheinberg, “Visual object recognition,” *Annual Review of Neuroscience*, vol. 19, no. 1, pp. 577–621, 1996.
- [45] S. Z. Li, X. Hou, H. Zhang, and Q. Cheng, “Learning spatially localized, parts-based representation,” in *IEEE International Conference on Computer Vision (CVPR)*, 2001, pp. 207–212.
- [46] R. Sandler *et al.*, “Nonnegative matrix factorization with earth mover’s distance metric for image analysis,” *IEEE Transactions on Pattern Analysis and Machine Intelligence (PAMI)*, vol. 33, no. 8, pp. 1590–1602, 2011.
- [47] W. Xu, X. Liu, and Y. Gong, “Document clustering based on non-negative matrix factorization,” in *International Conference on Research and Development in Information Retrieval (SIGIR)*, 2003, pp. 267–273.
- [48] F. Shahnaz, M. W. Berry, V. P. Pauca, and R. J. Plemmons, “Document clustering using nonnegative matrix factorization,” *Elsevier Journal Information Processing & Management*, vol. 42, no. 2, pp. 373–386, 2006.
- [49] D. D. Lee and H. S. Seung, “Algorithms for non-negative matrix factorization,” in *Advances in Neural Information Processing Systems (NIPS)*. MIT Press, 2000, pp. 556–562.
- [50] D. Lungu, S. Prasad, M. M. Crawford, and O. K. Ersoy, “Manifold-learning-based feature extraction for classification of hyperspectral data: A review of advances in manifold learning,” *IEEE Signal Process. Mag.*, vol. 31, no. 1, pp. 55–66, 2014.
- [51] P. O. Hoyer, “Non-negative sparse coding,” in *IEEE Workshop Neural Networks for Signal Processing*, 2002, pp. 557–565.
- [52] R. Tibshirani, “Regression shrinkage and selection via the lasso,” *Journal of the Royal Statistical Society*, vol. 58, no. 1, pp. 267–288, 1996.
- [53] D. L. Donoho, “Compressed sensing,” *IEEE Transactions Information Theory*, vol. 52, no. 4, pp. 1289–1306, 1996.
- [54] J. Fan and R. Li, “Variable selection via nonconcave penalized likelihood and its oracle properties,” *Journal of the American Statistical Association*, vol. 96, no. 456, pp. 1348–1360, 2001.
- [55] F. Nie, H. Huang, X. Cai, and C. H. Ding, “Efficient and robust feature selection via joint $\ell_{2,1}$ -norms minimization,” in *Advances in Neural Information Processing Systems (NIPS)*. Curran Associates, Inc., 2010, pp. 1813–1821.
- [56] H. Wang, F. Nie, and H. Huang, “Robust distance metric learning via simultaneous l_1 -norm minimization and maximization,” in *International Conference on Machine Learning (ICML)*, T. Jebara and E. P. Xing, Eds. JMLR Workshop and Conference Proceedings, 2014, pp. 1836–1844.
- [57] J. Fan and H. Peng, “Non-concave penalized likelihood with a diverging number of parameters,” *Annals of Statistics*, vol. 32, no. 3, pp. 928–961, 2004.
- [58] F. Nie, H. Wang, H. Huang, and C. H. Q. Ding, “Early active learning via robust representation and structured sparsity,” in *International Joint Conference on Artificial Intelligence (IJCAI)*, 2013, pp. 1572–1578.
- [59] K. Yu, J. Bi, and V. Tresp, “Active learning via transductive experimental design,” in *International Conference on Machine Learning*. New York, NY, USA: ACM, 2006, pp. 1081–1088.
- [60] G. Cheng, F. Zhu, S. Xiang, Y. Wang, and C. Pan, “Semisupervised hyperspectral image classification via discriminant analysis and robust regression,” *IEEE J. of Selected Topics in Applied Earth Observations and Remote Sensing*, vol. 9, no. 2, pp. 595–608, 2016.
- [61] Y. Wang, C. Pan, S. Xiang, and F. Zhu, “Robust hyperspectral unmixing with correntropy-based metric,” *IEEE Transactions on Image Processing*, vol. 24, no. 11, pp. 4027–4040, 2015.
- [62] N. Hurley and S. Rickard, “Comparing measures of sparsity,” *IEEE Transactions on Information Theory*, vol. 55, no. 10, pp. 4723–4741, Oct. 2009.
- [63] H. Li, S. Tak, and J. C. Ye, “Lipschitz-killing curvature based expected euler characteristics for p-value correction in fnirs,” *Journal of neuroscience methods*, vol. 204, no. 1, p. 61–67, February 2012.
- [64] J. Nocedal and S. J. Wright, *Numerical Optimization*, 2nd ed. New York: Springer, 2006.
- [65] C.-J. Lin, “Projected gradient methods for nonnegative matrix factorization,” *Neural Computation*, vol. 19, no. 10, pp. 2756–2779, 2007.
- [66] F. Zhu, “Hyperspectral unmixing datasets & ground truths on http://www.escience.cn/people/feiyunZHU/Dataset_GT.html,” 2014.
- [67] —, “Spectral unmixing datasets with ground truths,” *arXiv:1708.05125*, 2017.
- [68] C. Rodarmel and J. Shan, “Principal component analysis for hyperspectral image classification,” *Surveying and Land Information Science*, vol. 62, no. 2, p. 115, 2002.
- [69] H. M. Vargas and H. A. Fuentes, “Colored coded-apertures for spectral image unmixing,” in *SPIE Remote Sensing*. International Society for Optics and Photonics, 2015, pp. 964 320–964 320.
- [70] L. Tong, J. Zhou, Y. Qian, X. Bai, and Y. Gao, “Nonnegative-matrix-factorization-based hyperspectral unmixing with partially known endmembers,” *IEEE Transactions on Geoscience and Remote Sensing*, vol. 54, no. 11, pp. 6531–6544, 2016.
- [71] Z. Shu, J. Zhou, L. Tong, X. Bai, and C. Zhao, “Multilayer manifold and sparsity constrained nonnegative matrix factorization for hyperspectral unmixing,” in *Image Processing (ICIP), 2015 IEEE International Conference on*. IEEE, 2015, pp. 2174–2178.
- [72] L. Tong, J. Zhou, X. Li, Y. Qian, and Y. Gao, “Region-based structure preserving nonnegative matrix factorization for hyperspectral unmixing,” *IEEE Journal of Selected Topics in Applied Earth Observations and Remote Sensing*, vol. 10, no. 4, pp. 1575–1588, 2017.
- [73] S. Vasuki *et al.*, “Clustering based band selection for endmember extraction using simplex growing algorithm in hyperspectral images,” *Multimedia Tools and Applications*, vol. 76, no. 6, pp. 8355–8371, 2017.
- [74] V. S. K. Ganesan and S. Vasuki, “Maximin distance based band selection for endmember extraction in hyperspectral images using simplex growing algorithm,” *Multimedia Tools and Applications*, pp. 1–17.
- [75] Y. Fu, J. Gao, X. Hong, and D. Tien, “Low rank representation on riemannian manifold of square root densities,” *arXiv preprint arXiv:1508.04198*, 2015.
- [76] H. K. Aggarwal and A. Majumdar, “Hyperspectral unmixing in the presence of mixed noise using joint-sparsity and total variation,” *IEEE Journal of Selected Topics in Applied Earth Observations and Remote Sensing*, vol. 9, no. 9, pp. 4257–4266, 2016.
- [77] A. Agathos, J. Li, J. M. Bioucas-Dias, and A. Plaza, “Robust minimum volume simplex analysis for hyperspectral unmixing,” in *Signal Processing Conference (EUSIPCO), 2014 Proceedings of the 22nd European*. IEEE, 2014, pp. 1582–1586.
- [78] Q. Wei, M. Chen, J.-Y. Tourneret, and S. Godbill, “Unsupervised nonlinear spectral unmixing based on a multilinear mixing model,” *IEEE Transactions on Geoscience and Remote Sensing*, 2017.
- [79] S. Bernabé, G. Botella, G. Martín, M. Prieto-Matias, and A. Plaza, “Parallel implementation of a full hyperspectral unmixing chain using opencl,” *IEEE Journal of Selected Topics in Applied Earth Observations and Remote Sensing*, vol. 10, no. 6, pp. 2452–2461, 2017.
- [80] X. Wang, Y. Zhong, L. Zhang, and Y. Xu, “Spatial group sparsity regularized nonnegative matrix factorization for hyperspectral unmixing,” *IEEE Transactions on Geoscience and Remote Sensing*, 2017.
- [81] W. Wang, Y. Qian, and Y. Y. Tang, “Hypergraph-regularized sparse nmf for hyperspectral unmixing,” *IEEE Journal of Selected Topics in Applied Earth Observations and Remote Sensing*, vol. 9, no. 2, pp. 681–694, 2016.
- [82] E. Martel, R. Guerra, S. López, and R. Sarmiento, “A gpu-based processing chain for linearly unmixing hyperspectral images,” *IEEE Journal of Selected Topics in Applied Earth Observations and Remote Sensing*, vol. 10, no. 3, pp. 818–834, 2017.
- [83] K. Canham, A. Schlamm, A. Ziemann, B. Basener, and D. W. Messinger, “Spatially adaptive hyperspectral unmixing,” *IEEE Transactions on Geoscience and Remote Sensing (TGRS)*, vol. 49, no. 11, pp. 4248–4262, 2011.
- [84] F. Nie, H. Wang, X. Cai, H. Huang, and C. Ding, “Robust matrix completion via joint Schatten p-norm and lp-norm minimization,” in *IEEE International Conference on Data Mining (ICDM)*, Washington, DC, USA, 2012, pp. 566–574.